ROYAL SOCIETY
OF CHEMISTRY

EDGE ARTICLE

🔴 Check for updates

All publication charges for this article have been paid for by the Royal Society of Chemistry

Insights into the halogen-induced p-band center regulation promising high-performance lithium–sulfur batteries†

Hanzhang Fang,[a] Wenshuo Hou,*[a] Chuanlong Li,[a] Shuo Li,[a] Fulu Chu, [ID][a] Xuting Li,[a] Xianping Zhang,*[b] Linrui Hou, [ID][a] Changzhou Yuan [ID]*[a] and Yanwei Ma [ID][b]

Sn-based halide perovskites are expected to solve the problems of the shuttle effect and sluggish redox kinetics of lithium polysulfides (LiPSs) in lithium–sulfur batteries (LSBs) due to their high conductivity and electrocatalytic activity, but their intrinsic catalytic mechanism for LiPSs remains to be explored. Herein, halide perovskites with varying halide anions, Cs_2SnX_6 (X = Cl, Br, I), are purposefully designed to unveil the halogen-induced regulatory mechanism. Theoretical calculations demonstrate that increasing the halogen atomic number induces the shift of the p-band center closer to the Fermi level, which results in the localized charge distribution around halide anions and rapid charge separation/transfer at Sn sites, enhancing the adsorptive and catalytic activity and redox kinetics of LiPSs. Experimental investigations exhibit that LSBs assembled with the Cs_2SnI_6 modified separator deliver a high initial capacity of 1000 mA h g^{-1} at 2C, with a minimum decay rate of 0.068% per cycle after 500 cycles. More impressively, the Cs_2SnI_6 battery with a high sulfur loading (6.1 mg cm^{-2}) and a low electrolyte/sulfur ratio (5.5 μL mg^{-1}) achieves a remarkable reversible capacity of 768.8 mA h g^{-1}, along with robust wide-temperature-tolerant cycling performance from −20 to 50 °C. These findings underscore the critical role of p-band center regulation in rationally designing advanced LSBs.

1. Introduction

Lithium–sulfur batteries (LSBs) have been developed for next-generation energy storage because of their high theoretical capacity (1675 mA h g^{-1}), high energy density (2600 W h kg^{-1}), low cost and environmental friendliness when compared to lithium-ion batteries.[1–3] However, the industrial application of LSBs has been hindered seriously by several challenging bottlenecks. For example, due to the low conductivity of sulfur species and Li$_2$S/Li$_2$S$_2$, the "shuttle effect", which is caused by the dissolution of lithium polysulfides (LiPSs) in the electrolyte, leads to unsatisfactory actual capacity and cycling stability of LSBs. In addition, the sluggish conversion kinetics of LiPS also lead to a rapid decrease in the cycling capability of LSBs.[4–6] The shuttle effect and sluggish conversion kinetics of LiPSs in LSBs can be mitigated by constructing cathode materials,[7] designing multifunctional composite separators,[8] and optimizing electrolytes and lithium anodes.[9] Among them, the most critical aspect of separator design has been identified as the

introduction of electrocatalytic materials that have both adsorption and catalytic properties toward LiPSs, which can effectively address the challenges mentioned above faced by LSBs.[10,11]

In previous research studies, various polar and non-polar electrocatalytic materials have been explored to adsorb LiPSs and catalyze their redox reactions,[12–21] including metal oxides,[22] metal phosphides,[23] and metal sulfides.[24] Among them, oxide perovskites demonstrate good adsorptive and catalytic effects on LiPSs through their ferroelectric effect.[25] For instance, oxide perovskites such as LaNiO$_3$,[26] SrTiO$_3$,[27] and the layered double perovskite PrBaCo$_2$O$_6$[28] have been utilized to fabricate separators for LSBs. These oxide perovskites inhibit the shuttle effect and promote the conversion of LiPSs. However, oxide perovskites still face challenges related to a lack of active sites and poor conductivity.[29] In practical applications, the conductivity and electrocatalytic activity of electrocatalytic materials can be enhanced by adjusting their surface electronic state and the rate of charge transfer. Halide perovskites are known for their superior charge transport properties, tunable band structure, and high defect tolerance, which endow them with excellent electrocatalytic activity.[30–34] Halide perovskites can also regulate structural characteristics by altering the material composition. However, the presence of toxic lead in the chemical composition of most halide perovskites and their structural instability remain the two main

School of Materials Science & Engineering, University of Jinan, Jinan, 250022, P. R. China. E-mail: mse_houws@ujn.edu.cn; mse_yuancz@ujn.edu.cn; ayuancz@163.com
Institute of Electrical Engineering and Advanced Electromagnetic Drive Technology, Qilu Zhongke, Jinan 250013, P. R. China. E-mail: zxp@mail.iee.ac.cn
† Electronic supplementary information (ESI) available. See DOI: https://doi.org/10.1039/d5sc01266j

limiting factors hindering their application.[35] Compared to other halide perovskites, halide double perovskites possess a greater number of halogen active sites and exhibit enhanced chemical stability in air and polar solutions. In contrast, halide perovskites are prone to oxidation in air and react with water and polar solutions.[36] Traditional lead-based halide perovskites have restricted applications due to the toxicity of lead. Sn-based halide double perovskites are environmentally friendly and have a narrower band gap than other metal-based halide perovskites, which render better conductivity to them.[37] Moreover, by regulating the p-band center, higher ion/electron conductivity can be achieved, which helps to improve the adsorption and catalytic performance toward LiPSs. To date, the exploration of p-band center regulation of Sn-based halide double perovskites and their application in LSBs has been limited, particularly lacking in-depth investigations into the intrinsic mechanism of halide anions catalyzing LiPS conversion at the atomic scale.

With these comprehensive considerations in mind, in this contribution, we have purposefully constructed a series of Sn-based halide double perovskites with different halide anions, Cs_2SnX_6 (X = Cl, Br, I), to explore the regulatory mechanism of halide anions on the electronic structure. Both theoretical calculations and experimental results coherently confirmed that the p-band center of halogen anions shifted positively toward the Fermi level with the increase in the halogen atomic number. Such a unique electronic structural change endowed the material with remarkable electrocatalytic performance due to several advantages it possesses. Specifically, the I atoms in Cs_2SnI_6 first promoted the p-band center to be closer to the Fermi level, resulting in a higher charge transfer rate, which was more beneficial for catalyzing the conversion of LiPSs. Second, Cs_2SnI_6 achieved more localized charge distribution around the I atom, rendering a weaker charge distribution at the Sn center and promoting charge separation and transfer, which benefited the adsorptive and catalytic reactions of LiPSs on its surface. Third, the binding energy between Cs_2SnI_6 and LiPSs was higher than the other two counterparts, while Cs_2SnI_6 had the lowest energy barriers for LiPSs and Li_2S decomposition reactions. As a result, Cs_2SnI_6 exhibited excellent adsorption and catalytic conversion capability for LiPSs. The initial specific capacity of LSBs assembled with Cs_2SnI_6 modified separators was as high as 1000 mA h g^{-1} at 2C, along with a decay rate of only 0.068% after 500 cycles. Notably, the Cs_2SnI_6 battery with a high-S loading (6.1 mg cm^{-2}) and a low electrolyte/sulfur (E/S) ratio (5.5 µl mg^{-1}) still exhibited an extremely high capacity of 768.8 mA h g^{-1}. Additionally, the Cs_2SnI_6 battery exhibited initial capacities of 912.7 mA h g^{-1} at −20 °C at 0.1C and 1350.7 mA h g^{-1} at 50 °C at 0.5C, respectively. Encouragingly, the reversible capacities of 772.6 and 892.3 mA h g^{-1} could still be retained after 100 cycles at −20 at 50 °C, respectively. All in all, LSBs assembled with the Cs_2SnI_6 modified separator presented high reversible capacity and stable cycling performance, even under harsh operation conditions, including high sulfur loading, low E/S ratios, and extremely high/low working temperatures.

2. Experimental section

2.1. Preparation of materials

Sn-based halide double perovskites Cs_2SnX_6 (X = Cl, Br, I) were synthesized by a hydrothermal method. First, 0.947 g of tin acetate and 0.384 g of cesium acetate were dissolved in 10 mL of HX (X = Cl, Br, I) and stirred for 1 h. The mixed solution was transferred to a 25 mL autoclave and heated at 150 °C for 3 h. After being cooled to room temperature, the precipitate was collected by centrifugation, washed several times with isopropanol, and dried in a vacuum at 60 °C for 24 h. Then, the perovskite was ball-milled for 36 h to reduce the size of the perovskite particles.

2.2. Material characterization

The crystal structure of the original sample powder was characterized using a Rigaku Ultima IV XRD instrument produced by Rigaku Corporation (Cu-Kα radiation source; voltage, 40 kV; current, 20 mA; sweep speed, 1° or 10° min^{-1}). To obtain more detailed crystal structure data, the XRD data were refined using the Rietveld-refinement method and the General Structure Analysis System software. The microscopic morphology was analyzed using an FEI-Quanta FEG 250 field emission scanning electron microscope. The high-resolution microscopic morphology and structure of the material were observed using a JEM-2010F transmission electron microscope from JEOL Japan, and selected area electron diffraction (SAED) was conducted to observe the crystal plane composition. The element valence states were studied using XPS (Physical Electronics 5400 ESCA). The sulfur content in the cathode material was analyzed by thermogravimetry (TG, SDT 650).

2.3. Visualized adsorption of Li_2S_6

Li_2S_6 solution was prepared to characterize the adsorption properties of the material. S powder and Li_2S were mixed according to the stoichiometric ratio, dissolved in dimethyl ether, and stirred until transparent. The concentration of Li_2S_6 was 2.5 mmol L^{-1}. 0.1 mol of Cs_2SnX_6 (X = Cl, Br, I) was added to 4.0 mL of Li_2S_6/DME solution. After shaking for 1.0 min, the adsorption of Li_2S_6 on different adsorbents was observed after 6 h. The adsorption supernatant was diluted with dimethyl ether (1 : 8) and analyzed by ultraviolet spectroscopy. After adsorbing Li_2S_6, the material was dried in a glove box filled with Ar gas and subjected to XPS analysis.

2.4. Nucleation of Li_2S

S and Li_2S were mixed stoichiometrically and dissolved in a mixed solution of 1, 3-dioxopentane/dimethyl ether (v/v = 1/1) containing 1.0 mol per L lithium bis(trifluoromethanesulfonyl) imide (LiTFSI). Cs_2SnX_6 (X = Cl, Br, I) particles were ultrasonically dispersed in isopropyl alcohol and dropped on carbon paper to prepare Li_2S nucleation plates. The battery was assembled and discharged at a constant current of 0.112 mA to 2.10 V and then discharged at a constant voltage of 2.09 V until the current was lower than 10^{-5} A for Li_2S nucleation and

growth. According to Faraday's law, the charge of the whole process was calculated to evaluate the nucleation/growth rate of Li_2S.

2.5. Assembly and tests of Li_2S_6 symmetric cells

The carbon paper was cut into 12 mm discs, and ethanol dispersions of Cs_2SnX_6 (X = Cl, Br, I) particles were dropped onto the discs to fabricate symmetrical battery electrodes with a loading of 0.5 mg cm^{-2}. Two identical electrodes were assembled into a standard 2025 button cell containing 20.0 μL of Li_2S_6 (0.5 mol L^{-1} in [S]) and DOL/dimethyl ether (v/v = 1/1) electrolyte. The preparation method of the Li_2S_6 electrolyte was identical to that of the Li_2S_8 solution. Cyclic voltammetry (CV) curves of the above symmetrical cells were recorded between −0.8 and 0.8 V (Shanghai Chenhua CHI660e Electrochemical Workstation). The implemented scanning rate was 100 mV s^{-1}.

2.6. Cell assembly and electrochemical measurements

Cs_2SnI_6, carbon nanotubes (CNTs), and polyvinylpyrrolidone (PVP, K30) binder were uniformly mixed in isopropanol at a mass ratio of 6 : 3 : 1, and the resulting mixture was ultrasonically treated for 2 h, stirred for 3 h, and vacuum filtered onto the commercial Celgard 2500. The modified separator was prepared by drying at 60 °C and heating in an oven for 12 h. Control samples, Cs_2SnBr_6 modified separators, and Cs_2SnCl_6 modified separators (with the same mass ratio as the above samples) were prepared using the same procedure. Sulfur powder and Ketjen black (KB) were ground and mixed at a mass ratio of 3 : 1. The resulting mixture was transferred to a stainless steel high pressure vessel (50 mL) lined with polytetrafluoroethylene and heated at 155 °C for 12 h to obtain the KB and sulfur composite (KB/S). The cathode was prepared by uniformly mixing 80 wt% KB/S composite, 10 wt% Super P, and 10 wt% polyvinylidene difluoride (PVDF) binder in N-methyl-2-pyrrolidone (NMP). Then, the mixed slurry was scraped onto aluminum foil and dried at 60 °C for 12 h to obtain the S cathode. The S load was maintained at approximately 1.0 mg cm^{-2} (LA133 binder was used for the high sulfur loading tests). Next, the prepared S cathode, modified separator, and lithium anode were assembled into a CR2025 battery filled with Ar in a glove box. A 30 μL electrolyte containing 1 M LiTFSI was added to the battery, where LiTFSI was present in a mixed solvent of 1,2-dimethoxyethane and 1,3-dioxocyclopentene (1 : 1 in volume), containing 2% LiNO$_3$. The assembled battery was tested at room temperature using the LAND CT2001A battery test system. Cyclic voltammetry (CV) was performed on a CHI660E electrochemical workstation at a scan rate of 0.1 mV s^{-1}. Additionally, electrochemical impedance spectroscopy (EIS) tests were performed on the same instrument with an amplitude of 5 mV in a frequency range of 10 mHz to 100 kHz.

2.7. Computational details

The Perdew–Burke–Ernzerhof exchange–correlation generalized gradient approximation (GGA) was used for all computational structural relaxation processes in the study. Partial occupancies of the Kohn–Sham orbitals were allowed using the

Gaussian smearing method with a width of 0.05 eV. The electronic energy was considered self-consistent when the energy change was smaller than 10^{-5} eV. Geometry optimization was considered convergent when the energy change was smaller than 0.05 eV Å^{-1}. The Brillouin zone integration used $2 \times 2 \times 1$ Monkhorst–Pack k-point sampling for the structure. The adsorption energy (E_{ads}) was calculated as follows:

$$E_{ads} = E_{total} - E_{ad} - E_{sub} \qquad (1)$$

where E_{total}, E_{ad}, and E_{sub} represent the total energies of the optimized adsorbate/substrate system, the adsorbate in the structure, and the clean substrate, respectively. The free energy was calculated using the following equation:

$$\Delta G = \Delta E_{ads} + \Delta E_{zpe} - T\Delta S \qquad (2)$$

where ΔG, ΔE_{ads}, ΔE_{zpe}, and $T\Delta S$ represent the free energy and total energy from DFT calculations, zero point energy, and entropic contributions, respectively, where T was set to 300 K.

3. Results and discussion

3.1. Theoretical calculation and electronic structure analysis

As is well established, Cs_2SnX_6 (X = Cl, Br, I) exhibit a highly symmetrical cubic structure and possess excellent stability both in air and water, rendering them ideal candidates for exploring the regulatory mechanisms of halide anions.[33] Based on density functional theory (DFT), the electronic structure of Cs_2SnX_6 was investigated through density of states (DOS) and band structure calculations prior to the experiment. Halogen substitutions alter the bulk-phase configuration of Sn-based halide double perovskites. To demonstrate the intrinsic semiconducting properties through band structure and bandgap calculations, bulk-phase models were employed for DOS analysis.[38] Conversely, surface structural models were adopted for PDOS calculations to assess the p-band center of surface halogens, given that polysulfide adsorption and catalytic mechanisms in LSBs primarily operate at material surfaces.[39] The band gap and DOS for bulk Cs_2SnI_6 are presented in Fig. 1a. The simulated band gap value is 0.15 eV, corresponding to the DOS distribution, which is significantly smaller than those of bulk Cs_2SnBr_6 (1.36, Fig. 1b) and Cs_2SnCl_6 (2.53 eV, Fig. 1c). The electrical conductivity of bulk Cs_2SnX_6 increases as the band gap decreases, which is intimately linked to the electrochemical performance of LSBs. Notably, Cs_2SnI_6 exhibits the narrowest band gap, corresponding to the highest electrical conductivity. This structural feature significantly enhances the electron transport efficiency and is extremely advantageous for electrochemical reactions in LSBs. Given that the electrocatalytic reaction is essentially an electron transfer process, the valence electrons of elements, serving as electron donors or acceptors, exert a direct influence on the efficiency of electron transfer and play a pivotal role in electrocatalytic reactions.[40] For metal elements, their valence electrons are primarily electrons of d bands, while for nonmetal elements, their valence electrons are the p band electrons. The projected density of states (PDOS)
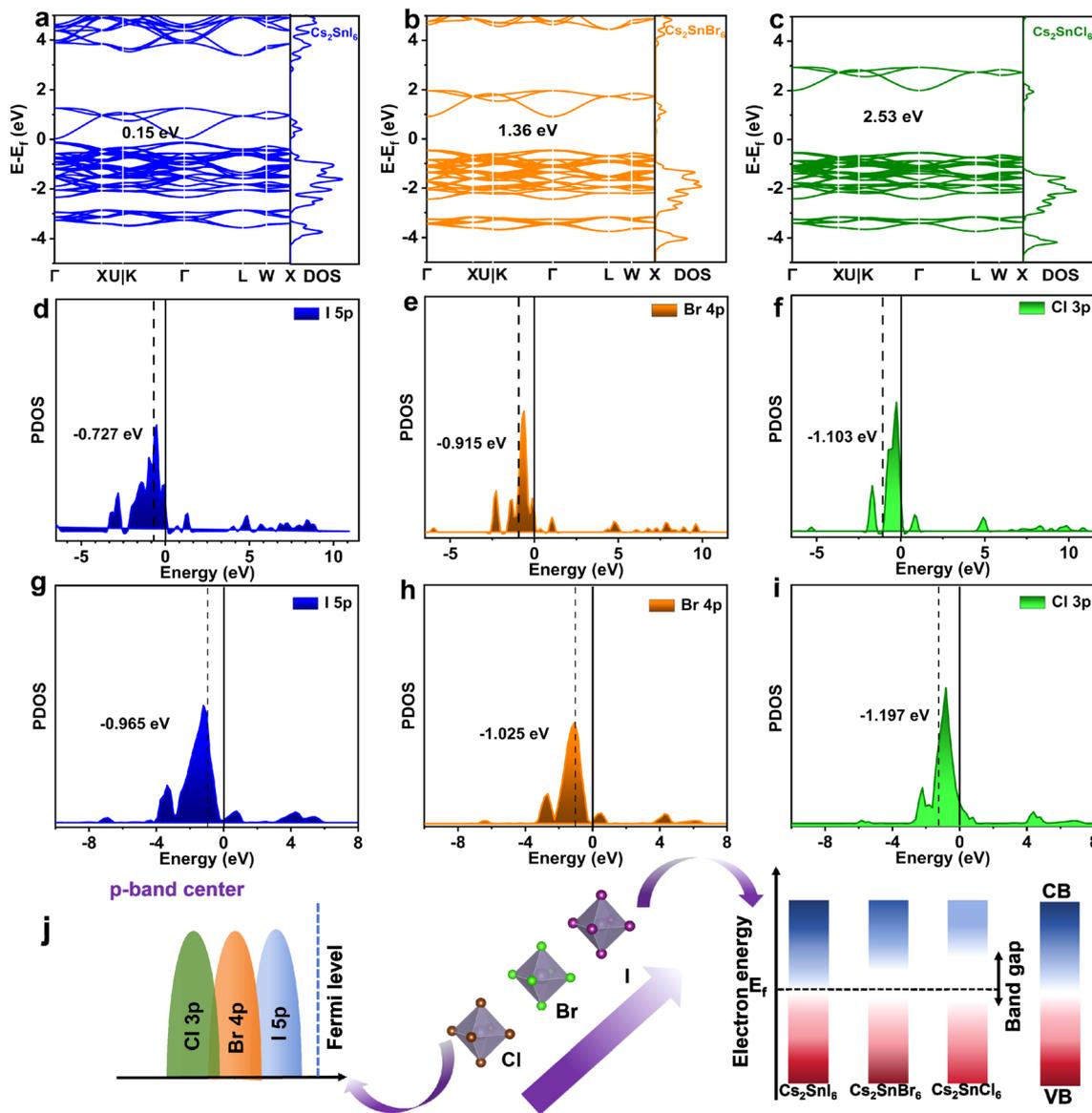
Fig. 1 DFT calculations of Cs_2SnX_6 (X = Cl, Br, I): electronic band structures of (a) Cs_2SnI_6, (b) Cs_2SnBr_6, and (c) Cs_2SnCl_6. (d–i) PDOS files of (d and g) I 5p, (e and h) Br 4p, and (f and i) Cl 3p for (d–f) fresh Cs_2SnX_6 and (g–i) after adsorbing Li_2S_6. (j) Schematic illustration of the p-band center regulation and electronic band structure of halide anions in Cs_2SnX_6.

of the p-band centers for nonmetal elements (Cl, Br, and I) was calculated to investigate the role of valence electrons in electrocatalytic reactions. The PDOS plots of I in Cs_2SnI_6 reveal that the calculated p-band center is located at −0.727 eV (Fig. 1d). By contrast, the p-band center of Br is centered at 0.915 eV for the case of Cs_2SnBr_6 (Fig. 1e). As for Cs_2SnCl_6, the calculated p-band center of Cl is −1.103 eV (Fig. 1f), positioned farthest from the Fermi level among the three. Clearly, as the halogen atomic number increases, the p-band centers move even closer to the Fermi level, which can potentially accelerate electron transfer.[41] The change in valence electrons of halogen elements facilitates the formation and cleavage of bonds during the redox process of LiPSs, ultimately enhancing the efficiency of the electrocatalytic process.[42]

During the charge–discharge cycles of LSBs, LiPSs are always adsorbed onto the surface of electrocatalysts Cs_2SnX_6. This process is accompanied by the redistribution of electrons between the electrocatalysts and LiPSs. The PDOS plot reveals that the p-band center of I in the Cs_2SnI_6–Li_2S_6 system is located at −0.727 eV (Fig. 1g), which is the closest to the Fermi level among the three systems. This electronic structural feature enhances the interaction between Cs_2SnI_6 and Li_2S_6, thereby facilitating the adsorption and activation of Li_2S_6. In the Cs_2SnBr_6–Li_2S_6 system, the p-band center of Br is located at −1.025 eV (Fig. 1h). In contrast, in the Cs_2SnCl_6–Li_2S_6 system, the p-band center of Cl is located at −1.197 eV (Fig. 1i), representing the most negative value among the three systems. The results here suggest that as the element changes from I to Cl, its p-band

center gradually shifts upwards and away from the Fermi level, which will weaken the interaction strength between the electrocatalyst and Li_2S_6, thereby resulting in decreased electrocatalytic performance. By investigating the interaction between Li_2S_6 and Cs_2SnX_6, the underlying mechanisms through which these electronic structure changes influence the electrocatalytic performance have been elucidated further. The schematic diagram (Fig. 1j) explicitly illustrates the regulatory mechanism of the p-band center and electronic structure induced by the halogen change in Cs_2SnX_6, where Cs_2SnCl_6, Cs_2SnBr_6, and Cs_2SnI_6 all exhibit octahedral structures. The transition of halide anions from Cl to I first causes a shift in the position of the p-band center relative to the Fermi level. As the atomic number of the halogen increases, the p-band center of the halide anion shifts toward the Fermi level, indicating an enhanced electron transfer rate, and consequently improves the electrocatalytic performance. Besides, the band gap also changes accordingly. The band gaps of the conduction band (CB) and valence band (VB) of Cs_2SnCl_6, Cs_2SnBr_6, and Cs_2SnI_6 gradually decrease, which leads to an increase in their conductivity. Overall, a series of theoretical calculations for Cs_2SnX_6 (X = Cl, Br, I) demonstrate that by contrapuntally adjusting the halogen composition in halide perovskites, the p-band center and electronic structure of halide anions can be effectively regulated, thereby improving the conductivity and electrocatalytic activity of the materials.

3.2. Physicochemical and structural characterization studies

To verify the theoretical calculation results mentioned above, a series of Sn-based halide double perovskites Cs_2SnX_6 (X = Cl, Br, I) with different halide anions were synthesized by a hydrothermal method.[43] Typical X-ray diffraction (XRD) patterns reveal that the diffraction peaks near $2\theta = 13°$, 26°, and 52° correspond to the (111), (222), and (622) crystal planes of Cs_2SnI_6 (JCPDS no. 73-0330), respectively (Fig. S1, ESI†). Additionally, the distinct and sharp peaks indicate a high degree of crystallinity in Cs_2SnI_6. Similar reflections are also observed for Cs_2SnBr_6 (JCPDS no. 97-8957, Fig. S1b, ESI†) and Cs_2SnCl_6 (JCPDS no. 75-0376, Fig. S1c, ESI†). It is noteworthy that after comparing XRD patterns of the three samples, the characteristic peak position shifts to even smaller angles with increasing halogen atomic number, featuring an increase in the unit cell volume of the samples. To determine their detailed crystal structures, the Rietveld method was employed to fit the experimental XRD data using GSAS/EXPGUI software. The low R_p and R_{wp} factors consistent with experimental data were obtained, demonstrating a high degree of fitting accuracy. Cs_2SnI_6 (Fig. 2a), Cs_2SnBr_6 (Fig. 2b), and Cs_2SnCl_6 (Fig. 2c) exhibit the same perovskite structure ($Fm\bar{3}m$) with lattice volumes of 1117, 1273, and 1577 $\mathring{A}^3$, respectively (Fig. S2, ESI†). It is observed that as the halogen atomic number increases, the lattice parameters a, b, and c also increase accordingly, leading to an expansion of the unit cell volume, which directly influences the structural
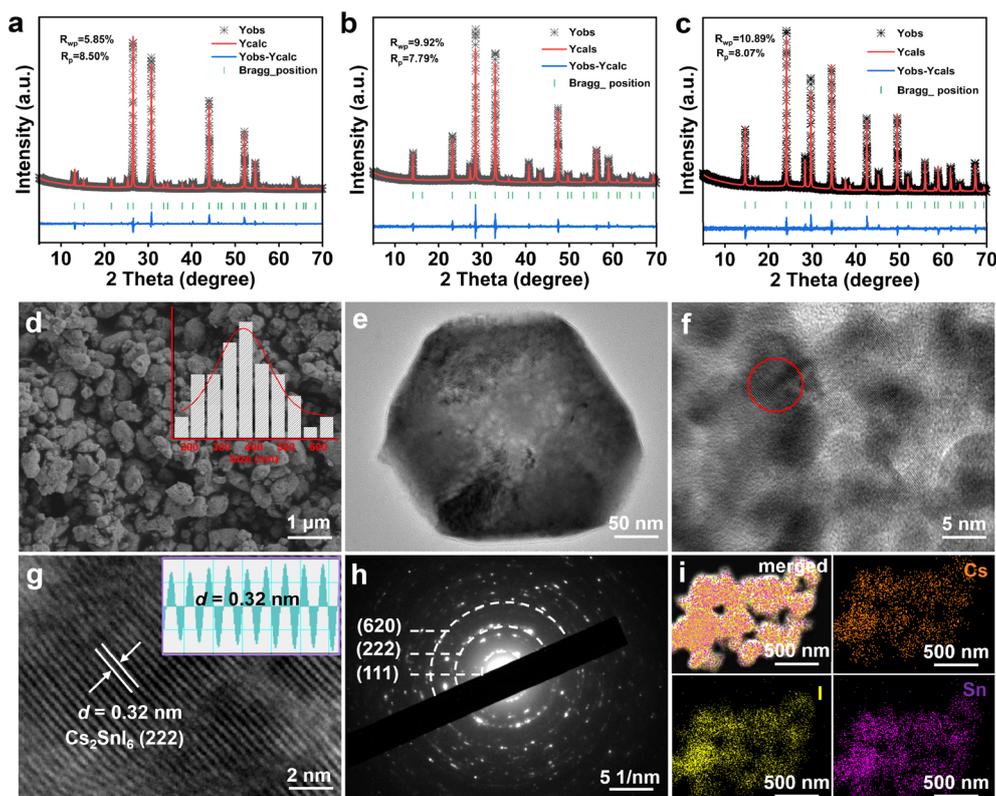

Fig. 2 XRD Rietveld refinement of (a) Cs_2SnI_6, (b) Cs_2SnBr_6, and (c) Cs_2SnCl_6. (d) FESEM, (e and f) TEM and (g) HRTEM images, (h) SAED pattern, and (i) EDS mapping images of Cs, Sn, and I elements for Cs_2SnI_6. The inset in panel (d) shows the particle size distribution diagram.

framework of the material. The expanded unit cell volume will boost ion diffusion and electron transport,[44] contributing to the improved electrochemical performance of LSBs.

Field emission scanning electron microscopy (FESEM), transmission electron microscopy (TEM), and high-resolution TEM (HRTEM) were conducted to elaborately investigate the morphological and structural evolution of the samples. FESEM observations (Fig. S3, ESI†) reveal that the as-prepared Cs_2SnCl_6, Cs_2SnBr_6, and Cs_2SnI_6 exhibit well-defined octahedral structures with particle size ranging approximately from 1 to 10 μm, and Cs_2SnI_6 presents the most uniform size distribution among them. Due to their micro-scale size, the subsequent ball-milling is highly necessary to obtain the nano-dimensional Cs_2SnX_6 samples before their application in LSBs. As noted, Cs_2SnI_6 forms uniform block shaped particles with sizes of approximately 200–500 nm after ball-milling (Fig. 2d). In contrast, the size of Cs_2SnBr_6 significantly decreases to ∼200 nm (Fig. S4a, ESI†), along with the smaller size of ∼100 nm for Cs_2SnCl_6 (Fig. S4b, ESI†), indicating that ball milling effectively reduces the particle size, which will contribute to its uniform distribution in the modified separator. The clear lattice fringes with a well-defined spacing of 0.32 nm, as presented in Fig. 2g,

correspond to the (222) crystal plane of Cs_2SnI_6, indicating its good crystallinity. Similarly, the well-discerned lattice fringes with spacings of 0.31 and 0.30 nm are easily identified and ascribed to the (222) crystal planes of Cs_2SnBr_6 (Fig. S5a, ESI†) and Cs_2SnCl_6 (Fig. S5b, ESI†), respectively. The variation trend in spacing follows the order of $Cs_2SnI_6 > Cs_2SnBr_6 > Cs_2SnCl_6$, which is in good agreement with the XRD refinement results presented above. Furthermore, the clear diffraction rings of the selected area electron diffraction (SAED) pattern (Fig. 2h) indicate the polycrystalline nature of Cs_2SnI_6, along with the well-indexed (111), (222), and (620) crystal planes. Similarly, both Cs_2SnBr_6 (Fig. S5c, ESI†) and Cs_2SnCl_6 (Fig. S5d, ESI†) exhibit polycrystalline features as well, owing to their multiple clear diffraction rings. Further elemental energy dispersive spectroscopy (EDS) mappings visualize the homogeneous distribution of Cs, Sn, and I throughout the Cs_2SnI_6 particles, as depicted in Fig. 2i. Correspondingly, EDS mappings (Fig. S6, ESI†) also authenticate the uniform distribution of Cs, Sn, and halogen elements (Br or Cl) in Cs_2SnBr_6 and Cs_2SnCl_6 particles. The uniform morphology, high crystallinity, and homogeneous elemental distribution of nanosized Cs_2SnX_6 particles jointly promote their excellent electrochemical performance in LSBs.
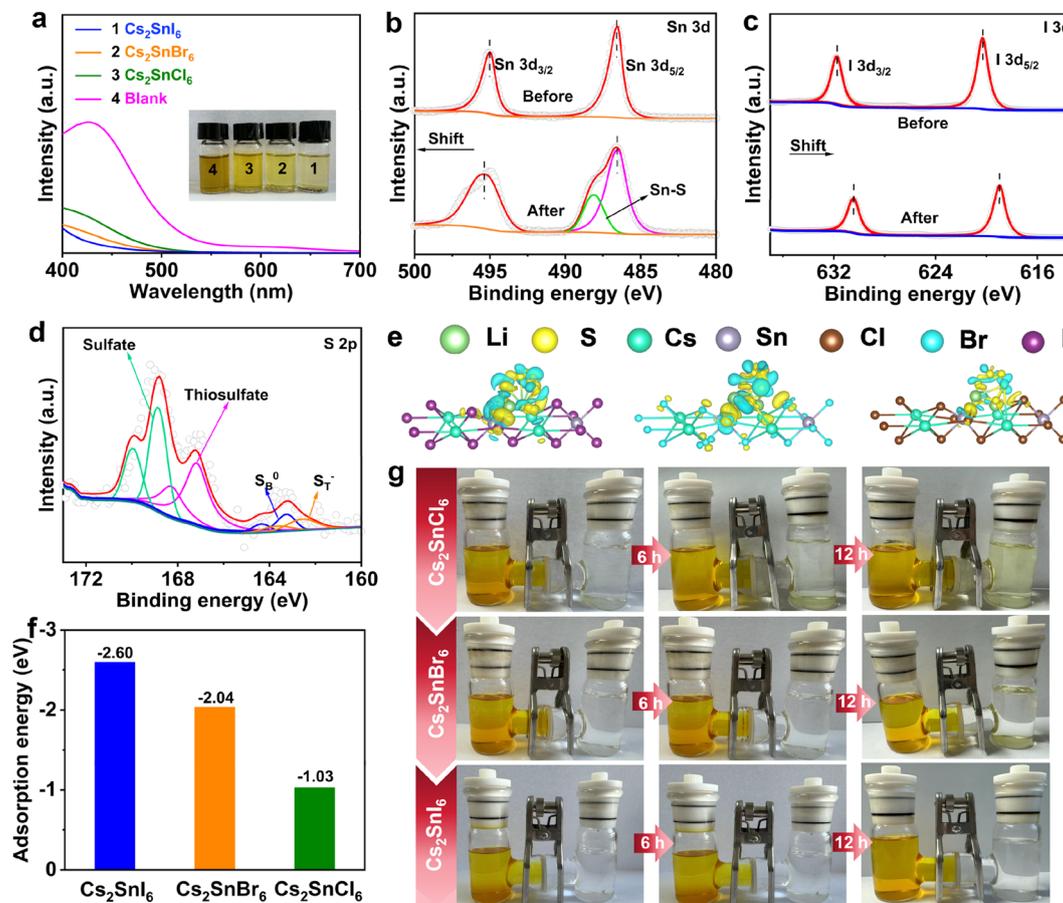

Fig. 3 (a) UV-vis spectra and the corresponding digital photos (inset) of Cs_2SnX_6 adsorbed Li_2S_6 after 12 h. High-resolution (b) Sn 3d and (c) I 3d spectra of Cs_2SnI_6 before and after adsorbing Li_2S_6, and (d) S 2p spectra of Cs_2SnI_6 absorbed with Li_2S_6. (e) Charge density difference analysis of Li_2S_6–Cs_2SnX_6. (f) Adsorption energy of Li_2S_6–Cs_2SnX_6. (g) Permeation tests of LiPSs in H-type electrolytic cells with Cs_2SnX_6 modified separators as indicated.

The adsorption capability of the four materials for LiPSs was compared through adsorption experiments in the Li_2S_6 solution (Fig. 3a). After 6 h, the yellow Li_2S_6 solution with Cs_2SnI_6 shows a nearly colorless appearance, highlighting its strongest absorbability to LiPSs among the three samples. The underlying reasons for this lie in the fact that Cs_2SnI_6 provides a certain adsorption capacity for Li_2S_6, as evidenced by the yellowish color of the Li_2S_6 solution containing Cs_2SnBr_6 and Cs_2SnCl_6. These intuitive results were further verified by UV-vis spectra, as the solution containing Cs_2SnI_6 exhibits the weakest signal of S_6^{2-} in the range of 400–500 nm.[45] The interactions between Cs_2SnX_6 and Li_2S_6 were further explored by high-resolution XPS before and after adsorption. Among them, the peaks at 486.8 eV and 495.2 eV are attributed to Sn^{4+}. After adsorption, the Sn 3d peaks shift to higher binding energies, from 486.8/495.2 eV to 486.9/495.4 eV, respectively. And a new pair of signals attributed to Sn–S bonds at 487.5 eV emerge, suggesting the facile anchoring of Li_2S_6 on Cs_2SnI_6.[46] The peak of the Sn–S bond appears in the Sn 3d XPS spectra of both Cs_2SnBr_6 (Fig. S7a, ESI†) and Cs_2SnCl_6 (Fig. S7b, ESI†). Notably, the Sn–S bond in Cs_2SnI_6 is the strongest among the three, indicating its strongest adsorption ability for Li_2S_6. Besides this, as shown in Fig. 3c, the peaks at 620.3 eV and 631.8 eV are attributed to I^-. After adsorbing Li_2S_6, the I 3d peaks shift toward lower binding energy, from 620.3/631.8 eV to 619.0/630.5 eV, revealing an interaction between I and Li_2S_6. The noticeable interactions between Li_2S_6 and Br/Cl are also detected, as such shifts are still found both in Br 3d (Fig. S7c, ESI†) and Cl 2p spectra (Fig. S7d, ESI†). It is especially mentioned that the shift in I 3d is the most pronounced, which means that the interaction between I and Li_2S_6 is the strongest among the halogens and explicitly confirms the superior adsorption capability of Cs_2SnI_6 toward LiPSs. Such characteristic interactions between the materials and LiPSs are further embodied in S 2p spectra of Cs_2SnX_6 absorbed with Li_2S_6 (Fig. 3c and S8, ESI†). Specifically, the two pairs of peaks in the high-binding-energy region (167.3–169.5 eV) correspond to sulfates and thiosulfates formed on the material surfaces through chemical interactions with LiPSs, and the other two pairs of peaks in the low-binding-energy region (161.8–163.7 eV) are related to the bridging sulfur (S_B^0) and terminal sulfur (S_T^-).[47] Compared with Cs_2SnBr_6 and Cs_2SnCl_6 (Fig. S8, ESI†), LiPSs captured on Cs_2SnI_6 (Fig. 3d) exhibit even higher peak intensities in the high-binding-energy region, further confirming the stronger chemical adsorption of Cs_2SnI_6 toward LiPSs from another point of view.[48]

To further analyze the regulatory mechanism of Cs_2SnX_6 (X = Cl, Br, I) on the adsorption of Li_2S_6, adsorptive models were constructed through DFT calculations (Fig. S9, ESI†). According to the DFT results, I and Sn atoms preferentially bond to Li and S atoms on LiPSs surface, which is consistent with the XPS analysis results presented above. Fig. 3e provides the charge density difference diagrams of Li_2S_6 adsorbed on different catalysts, where cyan and yellow correspond to charge depletion and accumulation, respectively. Apparently, the electron cloud density of the I center in Cs_2SnI_6 is higher than those of the Br center and Cl center, indicating that the contribution of halide anions to local charge distribution increases with the increase

of atomic number. Consequently, I anions in Cs_2SnX_6 act as a more active site. Cs_2SnI_6 achieves more local charge distribution at the I center, resulting in weaker charge distribution at the Sn center, thereby promoting charge separation and transfer and improving the conversion reaction kinetics of LiPSs. While the local charge distributions at the Br center and Cl center in Cs_2SnBr_6 and Cs_2SnCl_6 become weak, leading to the relatively slower conversion reaction kinetics of LiPSs. Additionally, Li_2S_6 has the adsorption energy of −2.60 eV on the Cs_2SnI_6 surface, which is higher than those of Cs_2SnBr_6 (−2.04 eV) and Cs_2SnCl_6 (−1.03 eV), as manifested in Fig. 3f. The results above indicate that the regulation of the halogen anion p-band center indeed enhances the electron transfer ability of Cs_2SnI_6 and strengthens its binding energy with LiPSs. Therefore, Cs_2SnI_6 can better capture LiPSs and suppress the shuttle effect more effectively.

The modified separators for LSBs were prepared by simply coating polypropylene (PP) with the nanosized Cs_2SnX_6 (X = Cl, Br, I). The Cs_2SnI_6, Cs_2SnBr_6, and Cs_2SnCl_6 modified separators were attached closely to PP with the thicknesses of 16.0, 14.3, and 15.0 μm, respectively (Fig. S10, ESI†).[49] Evidently, Cs_2SnX_6 (X = Cl, Br, I) and the conductive agent carbon nanotubes (CNTs) were observed to be uniformly distributed across the surface of the separator (Fig. S11, ESI†). The visible permeation experiment was carried out with H-type electrolyzers (Fig. 3g). Visually, LiPSs partially pass through the separator modified with Cs_2SnCl_6 just after 6 h, as evidenced by the initially colorless right chamber turning pale yellow. While the colorless transparent solutions are still observed in the right chambers for the cases of Cs_2SnBr_6 and Cs_2SnI_6 after 6 h, indicating that the inhibiting ability of the Cs_2SnBr_6 and Cs_2SnI_6 separators is indeed better than that of the Cs_2SnCl_6 separator. After 12 h, the electrolyte color turns out to be deepened in the right chamber of the Cs_2SnCl_6 separator, and a light yellow solution appears for the case of Cs_2SnBr_6. In sharp contrast, the electrolyte in the right chamber of the Cs_2SnI_6 separator always remains almost colorless even after the uninterrupted penetration/diffusion for 12 h, convincingly corroborating that the migration of LiPSs is effectively inhibited even at high LiPS concentrations, which is undoubtedly ascribed to the robust chemical adsorption capability of Cs_2SnI_6.[50]

3.3. Electrochemical evaluation

A symmetrical battery was assembled with Li_2S_6 electrolyte to measure the redox kinetics during the liquid–liquid conversion process. Notably, Cs_2SnI_6 exhibits the highest redox current response among the three samples (Fig. 4a), indicating that Cs_2SnI_6 significantly enhances the kinetics of the liquid–liquid conversion reaction. To further understand the superb function of our modified separators, electrochemical performance of LSBs assembled with KB/S (S content: 73.6 wt%) (Fig. S12, ESI†) as the cathode and metallic Li as the anode was systematically investigated. Cyclic voltammetry (CV) measurements were first carried out at a scanning rate of 0.1 mV s^{-1} in the voltage window from 1.7 to 2.8 V (vs. Li/Li$^+$), as plotted in Fig. 4b. The CV curve displays two distinct cathodic peaks at 2.33 V (peak 1)
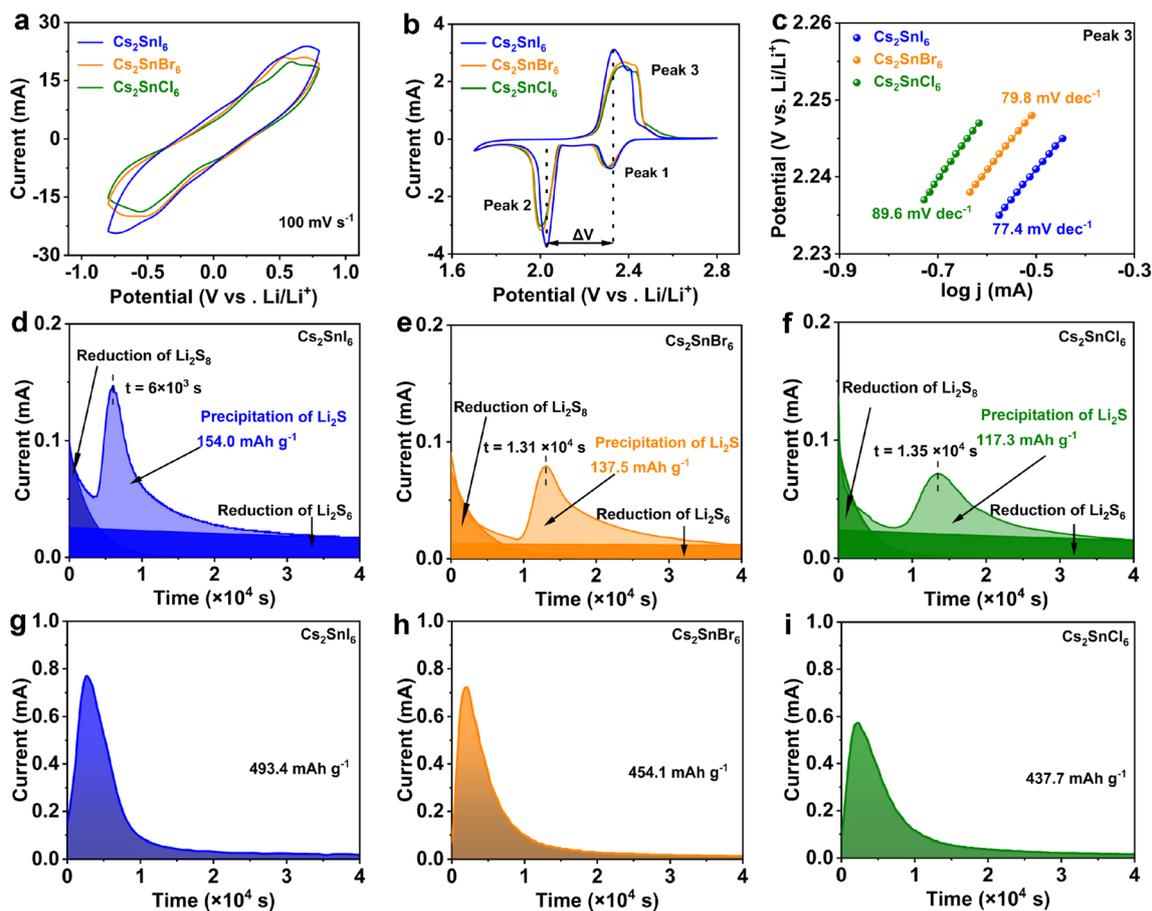
Fig. 4 CV curves of (a) Li_2S_6-symmetric batteries (100 mV s^{-1}) and (b) LSBs (0.1 mV s^{-1}) with Cs_2SnX_6 modified separators as indicated. (c) Tafel plots and slopes of peak 3 derived from the CV profiles. Fitted chronoamperometry curves of Li_2S (d–f) nucleation and (g–i) dissolution with different separators as indicated.

and 2.03 V (peak 2), corresponding to the reduction of the S_8 ring into soluble LiPSs (Li_2S_n, $4 \leq n \leq 8$) and further conversion into Li_2S_2/Li_2S.[51] Besides, the anodic peak appears at 2.34 V (peak 3), which is attributed to the desulfurization of Li_2S_2/Li_2S and Li_2S_n. Compared to reference samples of Cs_2SnBr_6 and Cs_2SnCl_6, the CV curve with the configured Cs_2SnI_6 battery shows the sharpest redox peak and the smallest overpotential (Fig. 4b). The local magnification of the oxidation and reduction peaks in the CV curve evidences that the Cs_2SnI_6 battery exhibits the highest peak current value, indicating that Cs_2SnI_6 has the best catalytic performance for both oxidation and reduction reactions in LSBs (Fig. S13, ESI†).[52] Moreover, the anodic peak of Cs_2SnI_6 exhibits an obvious negative shift, further depicting its efficient catalytic activity in accelerating the electrochemical activity of LiPSs.[53] To verify the reaction kinetics of different batteries, Tafel slopes were calculated by fitting the oxidation and reduction peak curves of Cs_2SnX_6 batteries. Specifically, the fitted Tafel slopes of the oxidation peaks for Cs_2SnI_6, Cs_2SnBr_6, and Cs_2SnCl_6 batteries are 77.4, 79.8, and 89.6 mV dec^{-1}, respectively (Fig. 4c). Additionally, the fitted Tafel slopes of the first reduction peaks for Cs_2SnI_6, Cs_2SnBr_6, and Cs_2SnCl_6 batteries are 49.0, 55.7, and 60.4 mV dec^{-1}, respectively

(Fig. S14a, ESI†). As for the second reduction peak, the fitted Tafel slopes for Cs_2SnI_6, Cs_2SnBr_6, and Cs_2SnCl_6 batteries are 28.3, 30.2, and 31.1 mV dec^{-1}, respectively (Fig. S14b, ESI†). Therefore, the smallest Tafel slopes for both oxidation and reduction reactions are observed in the Cs_2SnI_6 battery, highlighting the excellent catalytic performance of Cs_2SnI_6 for both oxidation and reduction reactions. This is attributed to the p-band center of I in Cs_2SnI_6, which is closer to the Fermi level; therefore, superior catalytic activities towards the redox reactions of sulfur species are obtained.

The electrochemical process in the discharge process involves both liquid–liquid and liquid–solid conversion reactions. To figure out the catalytic ability of Cs_2SnI_6 in the liquid–solid conversion process, the nucleation and decomposition behaviors of Li_2S on different Cs_2SnX_6 substrates were investigated by chronoamperometry. The response time of Li_2S nucleation (6000 s) in Cs_2SnI_6 (Fig. 4d) is significantly shorter than those of Cs_2SnBr_6 (13 100 s, Fig. 4e) and Cs_2SnCl_6 (13 500 s, Fig. 4f), revealing its faster nucleation rate. Moreover, Cs_2SnI_6 exhibits a higher nucleation capacity of 154.0 mA h g^{-1}, surpassing those of Cs_2SnBr_6 (137.5 mA h g^{-1}) and Cs_2SnCl_6 (117.3 mA h g^{-1}). The high nucleation ability of Li_2S authenticates that Cs_2SnI_6 effectively

catalyzes the liquid–solid conversion kinetics from Li_2S_4 to Li_2S. For the decomposition curve of Li_2S, Cs_2SnI_6 has the highest specific capacity of 493.4 mA h g^{-1} (Fig. 4g). By comparison, the lower Li_2S dissolution specific capacities are delivered by Cs_2SnBr_6 (454.1 mA h g^{-1}, Fig. 4h) and Cs_2SnCl_6 (437.7 mA h g^{-1}, Fig. 4i). These observations corroborate the superb ability of Cs_2SnI_6 to decompose Li_2S during the charging process, which is reasonably attributed to the more charge distribution at the I site in Cs_2SnI_6 after adsorbing LiPSs, thus exhibiting better catalytic activity.

The rate performance of the assembled LSBs was tested within the current rate range of 0.2–5C (1C = 1675 mA h g^{-1}). The capacities of LSBs using Cs_2SnI_6 modified separators at rates of 0.2, 0.5, 1, 2, 3, 4, and 5C were estimated as 1271, 1106, 997, 906, 876, 830, and 771 mA h g^{-1}, respectively (Fig. 5a). Upon switching back to 0.2C, a capacity as large as 1138 mA h g^{-1} can still be recovered, manifesting its admirable stability and high reversibility. The charge–discharge plots of the Cs_2SnI_6 battery present two clear plateaus evident even at a higher current rate of 5C, with a high-capacity response and a low polarization potential (Fig. 5b). Nevertheless, LSBs using Cs_2SnBr_6 and Cs_2SnCl_6 modified separators exhibited low capacities at the same rates (Fig. S15, ESI†). The excellent rate performance of the Cs_2SnI_6 battery is attributed to its outstanding adsorption and catalytic performance, which verifies the crucial role of halogen-induced p-band center
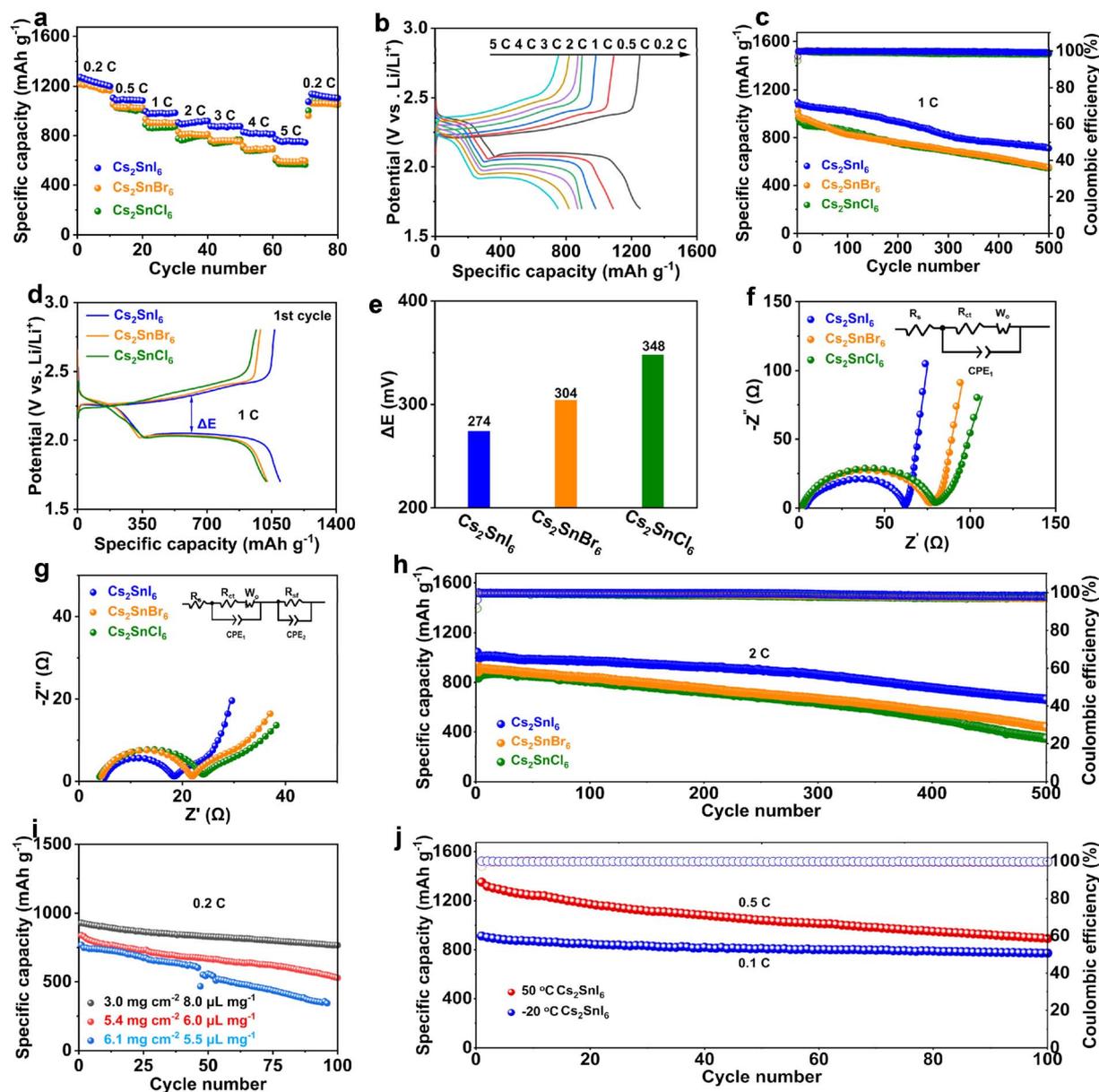

Fig. 5 (a) Rate performance and (b) charge–discharge curves of Cs_2SnX_6 batteries at different current densities. (c) Cycle stability, (d) the first charge–discharge plots, and (e) polarization overpotentials of Cs_2SnX_6 batteries at 1C. EIS data of Cs_2SnX_6 batteries (f) before and (g) after cycling at 1C. (h) Cycling stability of Cs_2SnX_6 batteries at 2C. Cycle stability of Cs_2SnI_6 batteries (i) under high loading and low E/S ratio conditions and (j) at different operating temperatures of 50 °C (0.5C) and −20 °C (0.1C).

regulation in Cs_2SnI_6. The cycling properties of LSBs with different separators at 1C are comparatively collected in Fig. 5c. An initial discharge capacity of 1097 mA h g^{-1} is achieved by LSBs using the Cs_2SnI_6 modified separator at 1C, and a retention capacity of 713 mA h g^{-1} is retained after 500 cycles, higher than those of LSBs with Cs_2SnBr_6 (1027 and 554 mA h g^{-1}) and Cs_2SnCl_6 separators (1021 and 543 mA h g^{-1}) under the same conditions. The fast capacity degradation of Cs_2SnBr_6 and Cs_2SnCl_6 batteries is ascribed to their poor adsorption and catalytic abilities toward LiPSs.

To investigate the influence of the mechanism of Cs_2SnX_6 with different anions on the battery performance, the charge–discharge plots of Cs_2SnI_6, Cs_2SnBr_6, and Cs_2SnCl_6 batteries at 1C rate were analyzed in detail. All the LSBs with different modified separators at 1C illustrate two distinct discharge platforms at 2.30 V and 2.05 V (Fig. 5d), which correspond to the electrochemical conversion of elemental sulfur to soluble polysulfides (Li_2S_n, $4 \leq n \leq 8$) based on the cathodic peaks observed in the CV curve (Fig. 4b), followed by reduction to insoluble Li_2S_2/Li_2S. Among them, the almost overlapping voltage platforms at different cycles are observed for the Cs_2SnI_6 battery (Fig. S16, ESI†), suggesting that the Cs_2SnI_6 modified separator has high sulfur redox chemical reversibility and cycling stability. The polarization overpotential of the Cs_2SnI_6 battery is 274 mV (Fig. 5e), even lower than those of Cs_2SnBr_6 (304 mV) and Cs_2SnCl_6 (348 mV). The observed smallest charge–discharge voltage hysteresis further suggests that Cs_2SnI_6 significantly enhances the catalytic activity for the conversion reaction of LiPSs, thereby improving the utilization of sulfur species.[54] As the atomic number of halogen increases, the adsorption and catalytic ability of Cs_2SnX_6 (X = Cl, Br, I) for LiPSs in the cathode region also increases. Consequently, the Cs_2SnI_6 modified separator achieves high-performance LSBs.

The resistance characteristics of Cs_2SnX_6 were further explored through electrochemical impedance spectroscopy (EIS) analysis. The Nyquist curves of batteries equipped with different separators were obtained before (Fig. 5f) and after cycling (Fig. 5g). All the EIS plots of LSBs consist of the intersections with the Z' axis, a semicircle in the middle frequency region and a tail line in the low-frequency region, corresponding to the solution resistance (R_s), charge-transfer resistance (R_{ct}) and Warburg impedance, respectively. Using the equivalent circuit diagrams (the insets), the fitted plots are found to be in good agreement with the experimental data, along with the fitting results (Table S1, ESI†). Clearly, all the Cs_2SnX_6 batteries display low R_s values ranging from 1.6 to 2.9 Ω. These low R_s values are attributed to the excellent conductivity of the modified separator, which effectively promotes electron and ion transport, thereby enhancing the performance of LSBs. Additionally, the R_{ct} of Cs_2SnI_6 battery is estimated as ~62.0 Ω, significantly lower than those of Cs_2SnBr_6 (76.0 Ω) and Cs_2SnCl_6 (78.6 Ω), indicating its superior charge transfer kinetics. As a result, the Cs_2SnI_6 modified separator will render the faster redox reactions of LiPSs and reduce the electrochemical reaction resistance.[55] More particularly, one additional semicircle appears in the high-medium frequency region of EIS plots for all batteries after cycling (Fig. 5g), which probably stems from the

extra surface film resistance (R_{sf}) caused by the formation of an insoluble Li_2S_2/Li_2S passivation layer on the electrode surface.[56,57] Despite this, the Cs_2SnI_6 battery still consistently exhibits the lowest R_{sf} and R_{ct} after cycling, suggesting the uniform deposition of Li_2S_2/Li_2S induced by Cs_2SnI_6, thanks to the superb adsorption and catalytic ability of Cs_2SnI_6 towards LiPSs.[58,59]

The shuttle effect in LSBs inevitably leads to adverse side reactions between lithium metal anodes and migrated LiPSs. To investigate the inhibitory effects of Cs_2SnI_6, Cs_2SnBr_6, and Cs_2SnCl_6 on LiPSs shuttle, LSBs were disassembled after 500 cycles at 1C. Noticeably, the distribution of sulfur species on the cathode surface of the Cs_2SnI_6 battery is relatively uniform, whereas the cathode surfaces of Cs_2SnBr_6 and Cs_2SnCl_6 batteries exhibited varying degrees of uneven sulfur deposition after cycling (Fig. S17, ESI†). Moreover, FESEM observations and the corresponding digital photographs indicate that the lithium anode in the Cs_2SnI_6 battery exhibits a smooth and dense surface after cycling (Fig. S18, ESI†).[60] In contrast, the lithium anode surfaces of Cs_2SnBr_6 and Cs_2SnCl_6 batteries show an undesirable loose structure, uneven lithium deposition, and numerous cracks, primarily caused by the migration of soluble LiPSs to the anode side.[61] In addition, the morphology of the cycled Cs_2SnI_6 modified separator (cathode side) remains largely unchanged, strongly confirming the good stability of the Cs_2SnI_6 separator during cycling (Fig. S19, ESI†). In summary, the Cs_2SnI_6 modified separator effectively suppresses the shuttle effect, which is mainly related to its excellent adsorption and catalytic properties for LiPSs. Subsequently, a long-cycle test was conducted at a high current rate to evaluate the long-cycle stability of the battery. At 2C, the initial capacity of the Cs_2SnI_6 battery remains as high as 1000 mA h g^{-1} (Fig. 5h), which is still kept at 660 mA h g^{-1} after 500 cycles, corresponding to a small capacity decay rate of only 0.068% per cycle. In sharp contrast, the Cs_2SnBr_6 and Cs_2SnCl_6 batteries display significant capacity degradation just after about 300 cycles. The higher cycling stability of the Cs_2SnI_6 battery is attributed to the modulation of the p-band center induced by halogen ions, which enhances LiPSs adsorption and catalytic ability of Cs_2SnI_6, thus effectively suppressing the shuttle effect of LiPSs.

The performance of LSBs assembled with the Cs_2SnI_6 modified separator under high sulfur load was further evaluated to check their potential application in high-energy-density devices. The gained initial capacities of Cs_2SnI_6 batteries with sulfur loadings of 3.0, 5.4, and 6.1 mg cm^{-2} at 0.2C are 928.6, 838.5, and 768.8 mA h g^{-1}, respectively. Typically, the charge–discharge curve of the Cs_2SnI_6 battery reveals two distinct plateaus even at a high sulfur loading of 6.1 mg cm^{-2} (Fig. S20a, ESI†). Under the conditions of sulfur loading of 3.0, 5.4, and 6.1 mg cm^{-2} and corresponding E/S ratio of 8.0, 6.0, and 5.5 μL mg^{-1}, the recorded charge–discharge plots of the Cs_2SnI_6 battery show almost overlapping voltage plateaus (Fig. S20b–d, ESI†), identifying that the separator modified by Cs_2SnI_6 has high sulfur redox chemical reversibility. Considering the multiscenario application of LSBs, their battery performance in extremely high and low temperature environments is also of

great significance. To evaluate this, cyclic performance tests were conducted on the Cs_2SnI_6 battery over a wide temperature range of −20 to 50 °C. The initial capacities of the Cs_2SnI_6 battery at −20 °C (0.1C) and 50 °C (0.5C) are 912.7 and 1350.7 mA h g^{-1}, respectively, coupled with the reversible capacities of 772.6 and 892.3 mA h g^{-1} after 100 cycles, respectively (Fig. 5j). Although the polarization overpotential of the Cs_2SnI_6 battery over the wide temperature range increases with decreasing temperatures (Fig. S21, ESI†), it still maintains a modest overpotential, which proves that the Cs_2SnI_6 battery can undergo rapid LiPS conversion over such a wide temperature range, guaranteeing its high initial specific capacity and excellent cycling stability even at extreme low and high temperatures. Compared with other electrocatalytic materials under the same testing conditions, the Cs_2SnI_6 battery exhibits excellent performance under long cycling (Table S2, ESI†), high sulfur loading, low E/S ratio (Table S3, ESI†), and extreme temperature conditions (Table S4, ESI†). The above electrochemical

performance tests established the regulatory relationship between different halide anions of Cs_2SnX_6 (X = Cl, Br, I) and electrochemical properties of LSBs. As the atomic number of the halogen increases, the rate performance, high-loading discharge capability, and cycling stability of LSBs are progressively enhanced. Among them, the Cs_2SnI_6 battery emanates superior electrochemical performance. Such distinctive improvement is primarily attributed to the effective adsorption of LiPSs by Cs_2SnI_6, which significantly suppresses the shuttle effect of LiPSs. Additionally, the inherent catalytic ability of Cs_2SnI_6 substantially accelerates the conversion reactions of LiPSs, further enhancing the overall electrochemical performance.

To thoroughly elucidate the specific catalytic mechanisms of Cs_2SnX_6 for the redox reactions of LiPSs, an atomic-level analysis was further carried out. Accordingly, the adsorption models of Cs_2SnX_6 with different LiPSs generated at various charge–discharge stages were constructed through DFT calculations.
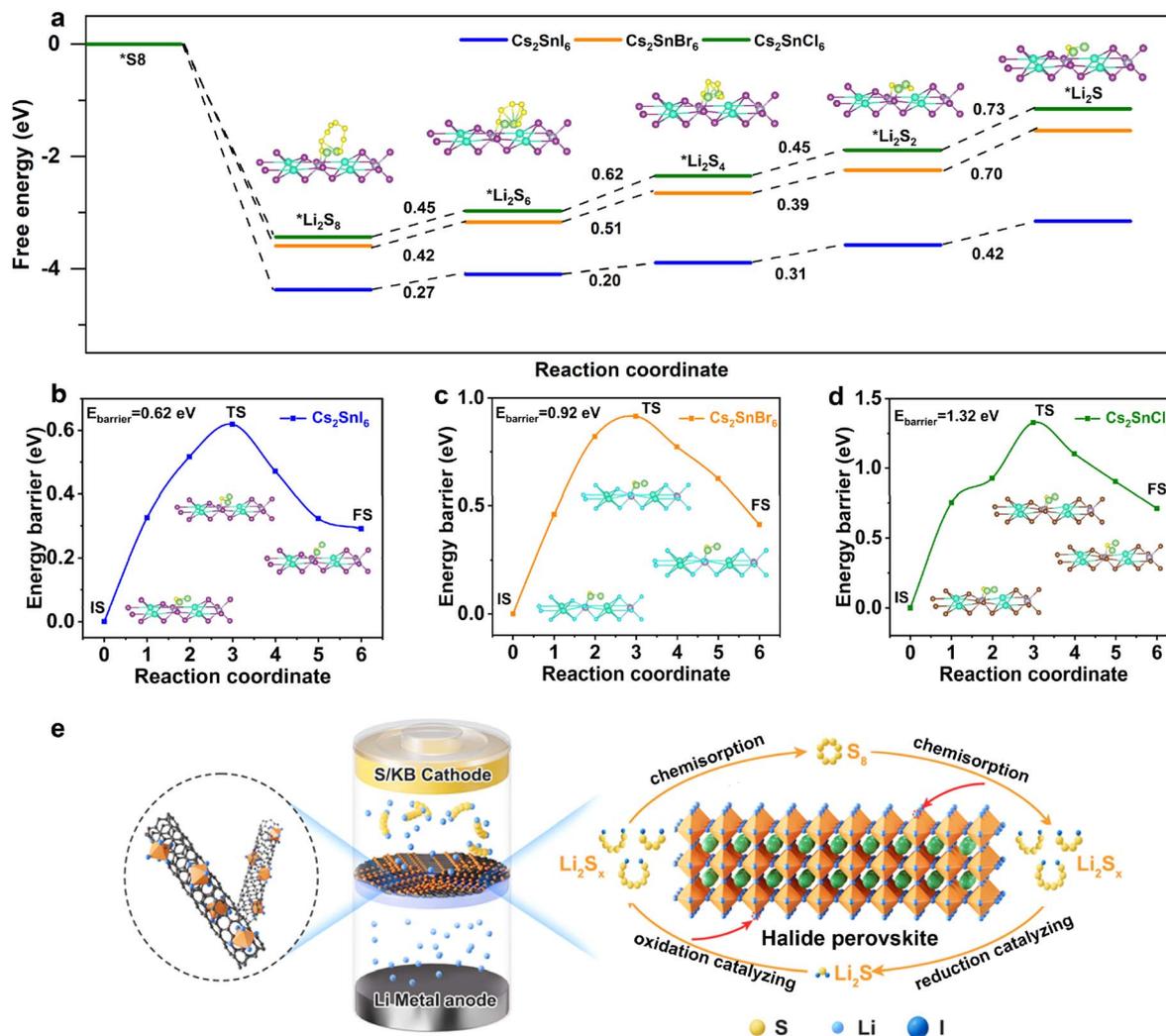

Fig. 6 (a) Relative free energy for reduction of sulfur species on the surfaces of Cs_2SnX_6. Energy barriers of Li_2S decomposition on the surfaces of (b) Cs_2SnI_6, (c) Cs_2SnBr_6, and (d) Cs_2SnCl_6. (e) Schematic illustration of the merits of the Cs_2SnI_6 modified separator inhibiting the "shuttle effect" in LSBs.

The Gibbs free energy distribution of Cs_2SnX_6 (X = Cl, Br, I) surfaces from S_8 to Li_2S is shown in Fig. 6a. The thermodynamic analysis of the continuous reduction pathway reveals that all transformation steps from Li_2S_8 to Li_2S exhibit positive Gibbs free energy changes, indicating the thermodynamically non-spontaneous characteristics, which necessitate the use of catalysts to facilitate LiPS conversion. Overall, the ΔG value of electrochemical reactions from Li_2S_8 to Li_2S in the Cs_2SnI_6 system is smaller than those in Cs_2SnBr_6 and Cs_2SnCl_6 systems, indicating that the electrochemical conversions of LiPSs are more favorable on the surface of Cs_2SnI_6. In particular, in the rate-limiting processes of liquid–solid conversion from Li_2S_4 to Li_2S_2 and solid–solid conversion from Li_2S_2 to Li_2S, the ΔG values of Cs_2SnI_6 are 0.31 and 0.42 eV, respectively, which are lower than those of Cs_2SnBr_6 (0.39 and 0.70 eV) and Cs_2SnCl_6 (0.45 and 0.84 eV), suggesting that the sulfur reduction reaction of Cs_2SnI_6 is thermodynamically more favorable. The decomposition of Li_2S is the first step in the charging process of LSBs and involves a solid–liquid phase transition, which results in relatively slow reaction kinetics. Consequently, the decomposition rate of Li_2S is critical to the charging process of LSBs. The calculated energy barriers for the decomposition of Li_2S on the surfaces of Cs_2SnX_6 (X = Cl, Br, I) reveal that Cs_2SnI_6 has a decomposition barrier of 0.62 eV (Fig. 6b), which is lower than those of Cs_2SnBr_6 (0.92 eV) (Fig. 6c) and Cs_2SnCl_6 (1.32 eV) (Fig. 6d). Such a finding fully substantiates that, during the charging process of LSBs, Li_2S undergoes accelerated dissociation on the surface of Cs_2SnI_6, which is in good agreement with the aforementioned electrochemical results. The calculation results show that the thermodynamic and kinetic processes can be improved by changing the halogen in the Sn-based halide double perovskite, which can simultaneously catalyze both the reduction of LiPSs and the oxidation of Li_2S. Specifically, as the atomic number of the halogen increases, the p-band center gradually approaches the Fermi level and the band gap decreases. These changes promote electron transfer, which is beneficial for the transformation of S species, thereby weakening the energy barriers in LiPSs reduction process and Li_2S oxidation process.

The action mechanism of the Cs_2SnI_6 modified separator in LSBs is schematically illustrated in Fig. 6e. Clearly, during the discharge process, a large amount of soluble LiPSs is present in the cathode region, while the anode region only contains Li^+. This demonstrates the effective inhibition of LiPSs shuttle by the Cs_2SnI_6 modified separator. The Cs_2SnI_6 modified separator effectively inhibits LiPSs shuttle due to its capability to chemically adsorb soluble LiPSs and the catalytic activity of surface I sites in promoting LiPSs conversion. The generated Li_2S can be uniformly distributed around the active sites. Additionally, the I sites on the surface of Cs_2SnI_6 also catalyze the oxidative reaction and decomposition of Li_2S, re-exposing the active sites for subsequent adsorption and catalysis. These structural characteristics of Cs_2SnI_6 modified separators ensure excellent catalytic effects on both oxidation and reduction reactions in LSBs, thereby effectively inhibiting LiPSs shuttle and enhancing the electrochemical performance of LSBs.

4. Conclusion

In summary, the regulatory mechanism of halogen-induced p-band centers and their effects on the adsorption and catalytic performance of LSBs were successfully explored through the research model of Sn-based halide perovskites. By combining DFT calculations with electrochemical characterization, a quantitative relationship was established between the electronic structure characteristics of halide anions and the adsorption and catalytic performance of LiPSs. DFT calculations revealed the regulatory mechanism of the p-band center of halide anions and the catalytic mechanism of LiPSs conversion reaction. As the atomic number of the halogen increases, the p-band center of the halogen anion shifted positively toward the Fermi level, resulting in a higher charge transfer rate and promoting the kinetics of the conversion reaction of LiPSs. Meanwhile, Cs_2SnI_6 achieved a greater local charge distribution on the I center, leading to a weaker charge distribution at the Sn center and further promoting charge separation and transfer. Therefore, the binding energy between halide perovskites and LiPSs increased, the potential barrier for LiPSs decomposition decreased accordingly, and the phase transition speed of LiPSs increased. LSBs assembled with the Cs_2SnI_6 modified separator exhibited a high discharge capacity (1000 mA h g^{-1} at 2C), excellent rate performance (771.0 mA h g^{-1} at 5C), and long-term cycle stability (0.068% decay rate per cycle after 500 cycles at 2C). Even under extreme temperature conditions, the Cs_2SnI_6 battery maintained a high discharge capacity (912.7 mA h g^{-1} at 0.1C at −20 °C and 1350.7 mA h g^{-1} at 0.5C at 50 °C). In this contribution, the adsorption and catalytic performance of LiPSs were regulated by adjusting the p-band center in halide perovskites, providing a new approach for developing advanced LSBs through halogen-induced p-band center regulation engineering.

Data availability

The data supporting this article can be available from the authors upon request.

Author contributions

Hanzhang Fang: formal analysis, investigation, writing – original draft, writing – review & editing. Wenshuo Hou: formal analysis, writing – original draft, writing – review & editing, conceptualization, funding acquisition. Chuanlong Li: formal analysis, investigation. Shuo Li: formal analysis, investigation. Fulu Chu: validation, software, funding acquisition. Xuting Li: validation, writing – review & editing. Xianping Zhang: formal analysis, writing – review & editing, conceptualization. Linrui Hou: validation, software, funding acquisition. Changzhou Yuan: formal analysis, investigation, conceptualization, writing – review & editing, funding acquisition. Yanwei Ma: formal analysis.

Conflicts of interest

There are no conflicts to declare.

Acknowledgements

References

1 P. G. Bruce, S. A. Freunberger, L. J. Hardwick and J.-M. Tarascon, *Nat. Mater.*, 2012, **11**, 19–29.

2 X. Liang, C. Hart, Q. Pang, A. Garsuch, T. Weiss and L. F. Nazar, *Nat. Commun.*, 2015, **6**, 5682–5690.

3 M. Du, J. Shi, Y. Shi, G. Zhang, Y. Yan, P. Geng, Z. Tian and H. Pang, *Chem. Sci.*, 2024, **15**, 9775–9783.

4 G. Zhou, S. Wang, T. Wang, S. Z. Yang, B. Johannessen, H. Chen, C. Liu, Y. Ye, Y. Wu, Y. Peng, C. Liu, S. P. Jiang, Q. Zhang and Y. Cui, *Nano Lett.*, 2020, **20**, 1252–1261.

5 Z. Sun, J. Zhang, L. Yin, G. Hu, R. Fang, H.-M. Cheng and F. Li, *Nat. Commun.*, 2017, **8**, 14627–14635.

6 X. Jiao, X. Tang, J. Li, Y. Xiang, C. Li, C. Tong, M. Shao and Z. Wei, *Chem. Sci.*, 2024, **15**, 7949–7964.

7 Z. Yuan, H. J. Peng, J. Q. Huang, X. Y. Liu, D. W. Wang, X. B. Cheng and Q. Zhang, *Adv. Funct. Mater.*, 2014, **24**, 6105–6112.

8 M. Zhang, X. Zhang, S. Liu, W. Hou, Y. Lu, L. Hou, Y. Luo, Y. Liu and C. Yuan, *ChemSusChem*, 2024, **17**, e202400538.

9 W. Guo, W. Zhang, Y. Si, D. Wang, Y. Fu and A. Manthiram, *Nat. Commun.*, 2021, **12**, 3031–3044.

10 L. Zhang, D. Liu, Z. Muhammad, F. Wan, W. Xie, Y. Wang, L. Song, Z. Niu and J. Chen, *Adv. Mater.*, 2019, **31**, 1903955.

11 H. Zhang, R. Dai, S. Zhu, L. Zhou, Q. Xu and Y. Min, *Chem. Eng. J.*, 2022, **429**, 132454–132465.

12 F. Pei, L. Lin, A. Fu, S. Mo, D. Ou, X. Fang and N. Zheng, *Joule*, 2018, **2**, 323–336.

13 Y. Pang, J. Wei, Y. Wang and Y. Xia, *Adv. Energy Mater.*, 2018, **8**, 1702288.

14 R. Xu, H. Tang, Y. Zhou, F. Wang, H. Wang, M. Shao, C. Li and Z. Wei, *Chem. Sci.*, 2022, **13**, 6224–6232.

15 Y. Liu, S. Liu, G. Zhao, M. Shen, X. Gao, Y. Zhao, X. Liu, L. Hou and C. Yuan, *Angew. Chem., Int. Ed.*, 2025, **64**, e202420287.

16 G. Zhao, S. Liu, X. Zhang, Y. Zhang, H. Shi, Y. Liu, L. Hou and C. Yuan, *J. Mater. Chem. A*, 2023, **11**, 1856–1865.

17 L. Zhou, H. Pan, G. Yin, Y. Xiang, P. Tan, X. Li, Y. Jiang, M. Xu and X. Zhang, *Adv. Funct. Mater.*, 2024, **34**, 2314246.

18 Y. Liu, X. Gao, M. Shen, Y. Zhao, X. Zhang, S. Liu, X. Liu, L. Hou and C. Yuan, *Angew. Chem., Int. Ed.*, 2024, **63**, e202412898.

19 H. Yuan, T. Liu, Y. Liu, J. Nai, Y. Wang, W. Zhang and X. Tao, *Chem. Sci.*, 2019, **10**, 7484–7495.

20 Y. Li, Z. Chen, X.-Y. Zhong, T. Mei, Z. Li, L. Yue, J.-L. Yang, H. J. Fan and M. Xu, *Adv. Funct. Mater.*, 2025, **35**, 2412279.

21 C. Sun, J. Zhu, B. Liu, M. Xu, J. Jiang and T. Yu, *ACS Energy Lett.*, 2022, **8**, 772–779.

22 H. Cheng, S. Zhang, S. Li, C. Gao, S. Zhao, Y. Lu and M. Wang, *Small*, 2022, **18**, 2202557.

23 Z. Wu, S. Chen, L. Wang, Q. Deng, Z. Zeng, J. Wang and S. Deng, *Energy Storage Mater.*, 2021, **38**, 381–388.

24 Y. Li, Y. Hao, U. Ali, Q. Zhang, Z. Jin, H. Sun, L. Li, L. Zhang, C. Wang and B. Liu, *Chem. Eng. J.*, 2023, **474**, 145961–145970.

25 L. Kong, X. Chen, B. Q. Li, H. J. Peng, J. Q. Huang, J. Xie and Q. Zhang, *Adv. Mater.*, 2018, **30**, 1705219.

26 W. Wang, M. Hou, F. Han, D. Yu, J. Liu, Q. Zhang, F. Yu, L. Wang and M. He, *J. Energy Chem.*, 2023, **82**, 581–591.

27 W. Hou, P. Feng, X. Guo, Z. Wang, Z. Bai, Y. Bai, G. Wang and K. Sun, *Adv. Mater.*, 2022, **34**, 2202222.

28 Z. Bai, Z. Wang, R. Li, Z. Wu, P. Feng, L. Zhao, T. Wang, W. Hou, Y. Bai, G. Wang and K. Sun, *Nano Lett.*, 2023, **23**, 4908–4915.

29 Q. Li, D. Zhang, J. Wu, S. Dai, H. Liu, M. Lu, R. Cui, W. Liang, D. Wang, P. Xi, M. Liu, H. Li and L. Huang, *Adv. Mater.*, 2024, **36**, 2309266.

30 A. E. Maughan, A. M. Ganose, M. M. Bordelon, E. M. Miller, D. O. Scanlon and J. R. Neilson, *J. Am. Chem. Soc.*, 2016, **138**, 8453–8464.

31 B. Saparov, J. P. Sun, W. Meng, Z. Xiao, H.-S. Duan, O. Gunawan, D. Shin, I. G. Hill, Y. Yan and D. B. Mitzi, *Chem. Mater.*, 2016, **28**, 2315–2322.

32 B. Lee, C. C. Stoumpos, N. Zhou, F. Hao, C. Malliakas, C. Y. Yeh, T. J. Marks, M. G. Kanatzidis and R. P. H. Chang, *J. Am. Chem. Soc.*, 2014, **136**, 15379–15385.

33 T. Paul, A. Sahoo, S. Maiti, D. S. Gavali, R. Thapa and R. Banerjee, *ACS Appl. Mater. Interfaces*, 2023, **15**, 34726–34741.

34 H. Shin, B. M. Kim, T. Jang, K. M. Kim, D. H. Roh, J. S. Nam, J. S. Kim, U. Y. Kim, B. Lee, Y. Pang and T. H. Kwon, *Adv. Energy Mater.*, 2019, **9**, 1803243.

35 F. Igbari, Z. K. Wang and L. S. Liao, *Adv. Energy Mater.*, 2019, **9**, 1803150.

36 I. Lopez-Fernandez, D. Valli, C.-Y. Wang, S. Samanta, T. Okamoto, Y.-T. Huang, K. Sun, Y. Liu, V. S. Chirvony, A. Patra, J. Zito, L. De Trizio, D. Gaur, H.-T. Sun, Z. Xia, X. Li, H. Zeng, I. Mora-Sero, N. Pradhan, J. P. Martinez-Pastor, P. Mueller-Buschbaum, V. Biju, T. Debnath, M. Saliba, E. Debroye, R. L. Z. Hoye, I. Infante, L. Manna and L. Polavarapu, *Adv. Funct. Mater.*, 2024, **34**, 2307896.

37 W. Ke and M. G. Kanatzidis, *Nat. Commun.*, 2019, **10**, 965.

38 Z.-J. Cheng, S. Shao, B. Kim, T. A. Cochran, X. P. Yang, C. Yi, Y.-X. Jiang, J. Zhang, M. S. Hossain, S. Roychowdhury,

T. Yilmaz, E. Vescovo, A. Fedorov, C. Shekhar, C. Felser, G. Chang and Z. Hasan, *Phys. Rev. B*, 2024, **109**, 075150.

39 M. Fang, J. Han, S. He, J.-C. Ren, S. Li and W. Liu, *J. Am. Chem. Soc.*, 2023, **145**, 12601–12608.

40 X. Sun, R. B. Araujo, E. C. dos Santos, Y. Sang, H. Liu and X. Yu, *Chem. Soc. Rev.*, 2024, **53**, 7392–7425.

41 S. Xie, X. Chen, L. Wang, G. Zhang, H. Lv, G. Cai, Y.-R. Lu, T.-S. Chan, J. Zhang, J. Dong, H. Jin, X. Kong, J. Lu, S. Jin, X. Wu and H. Ji, *eScience*, 2024, **4**, 100222.

42 J. Zhou, X. Liu, L. Zhu, J. Zhou, Y. Guan, L. Chen, S. Niu, J. Cai, D. Sun, Y. Zhu, J. Du, G. Wang and Y. Qian, *Joule*, 2018, **2**, 2681–2693.

43 S. Stranks, G. Eperon, G. Grancini, C. Menelaou, M. Alcocer, T. Leijtens, L. Herz, A. Petrozza and H. Snaith, *Science*, 2013, **34241**, 341–344.

44 H. Duan, C. Wang, X.-S. Zhang, J. Fu, W. Li, J. Wan, R. Yu, M. Fan, F. Ren, S. Wang, M. Zheng, X. Li, J. Liang, R. Wen, S. Xin, Y.-G. Guo and X. Sun, *J. Am. Chem. Soc.*, 2024, **146**, 29335–29343.

45 L. Zhang, T. Li, X. Zhang, Z. Ma, Q. Zhou, Y. Liu, X. Jiang, H. Zhang, L. Ni and G. Diao, *J. Mater. Chem. A*, 2023, **11**, 3105–3117.

46 X. Wang, F. Li, W. J. Yin, Y. Si, M. Miao, X. Wang and Y. Fu, *Appl. Catal., B*, 2022, **304**, 120936–120946.

47 S. Hu, M. Yi, H. Wu, T. Wang, X. Ma, X. Liu and J. Zhang, *Adv. Funct. Mater.*, 2022, **32**, 2111084.

48 J. Chen, J. Lei, J. Zhou, X. Chen, R. Deng, M. Qian, Y. Chen and F. Wu, *Nano Res.*, 2024, **17**, 9651–9661.

49 H. Liu, W. H. Lai, H. L. Yang, Y. F. Zhu, Y. J. Lei, L. Zhao, J. Peng, Y. X. Wang, S. L. Chou and H. K. Liu, *Chem. Eng. J.*, 2021, **408**, 127348–127357.

50 P. Wang, X. Dai, P. Xu, S. Hu, X. Xiong, K. Zou, S. Guo, J. Sun, C. Zhang, Y. Liu, T. Zhou and Y. Chen, *eScience*, 2023, **3**, 100088.

51 X. Wu, R. Xie, D. Cai, B. Fei, C. Zhang, Q. Chen, B. Sa and H. Zhan, *Adv. Funct. Mater.*, 2024, **34**, 2315012.

52 K. Zou, X. Chen, W. Jing, X. Dai, P. Wang, Y. Liu, R. Qiao, M. Shi, Y. Chen, J. Sun and Y. Liu, *Energy Storage Mater.*, 2022, **48**, 133–144.

53 X. Song, C. Wang, Z. Shen, K. Guo, J. Wu, Z. Guo, X. Liu and Y. Zhao, *eScience*, 2024, **4**, 100225.

54 Y. Guo, J. Li, G. Yuan, J. Guo, Y. Zheng, Y. Huang, Q. Zhang, J. Li, J. Shen, C. Shu, J. Xu, Y. Tang, W. Lei and H. Shao, *ACS Nano*, 2023, **17**, 18253–18265.

55 G. Zhou, S. Pei, L. Li, D. Wang, S. Wang, K. Huang, L. Yin, F. Li and H. Cheng, *Adv. Mater.*, 2014, **26**, 625–631.

56 W. Zhang, F. Cheng, M. Wang, J. Xu, Y. Li, S. Sun, Y. Xu, L. Wang, L. Xu, Q. Li, C. Fang, Y. Lu and J. Han, *Adv. Funct. Mater.*, 2023, **33**, 2304008.

57 W. Tian, B. Xi, Z. Feng, H. Li, J. Feng and S. Xiong, *Adv. Energy Mater.*, 2019, **9**, 1901896.

58 W. Yao, W. Zheng, J. Xu, C. Tian, K. Han, W. Sun and S. Xiao, *ACS Nano*, 2021, **15**, 7114–7130.

59 C. Huang, J. Yu, C. Li, Z. Cui, C. Zhang, C. Zhang, B. Nan, J. Li, J. Arbiol and A. Cabot, *Adv. Funct. Mater.*, 2023, **33**, 2305624.

60 W. Tian, Z. Li, L. Miao, Z. Sun, Q. Wang and L. Jiao, *Adv. Mater.*, 2024, **36**, 2308586.

61 L. Fan, M. Li, X. Li, W. Xiao, Z. Chen and J. Lu, *Joule*, 2019, **3**, 361–386.